Materials Today Physics 20 (2021) 100467

Contents lists available at ScienceDirect

Materials Today Physics

journal homepage: https://www.journals.elsevier.com/materials-today-physics

Unprecedented pressure-driven metallization and topological charge transport in an anion radical salt

Sudeshna Samanta [b, c], Arun S. Nissimagoudar [d], Rabaya Basori [e], Alexei Kuzmin [f], Mingtao Li [b], Jinbo Zhang [g], Lin Wang [a, *], Yongjun Tian [a], Ho-kwang Mao [b]

[a] *Center for High Pressure Science (ChiPS), State Key Laboratory of Metastable Materials Science and Technology, Yanshan University, Qinhuangdao, Hebei, 066004, China*
[b] *Center for High Pressure Science and Technology Advanced Research, Shanghai, 201203, China*
[c] *School of Information Science and Technology, Fudan University, Shanghai, 200433, China*
[d] *Center for Superfunctional Materials, Department of Chemistry, School of Natural Science, Ulsan National Institute of Science and Technology (UNIST), Ulsan, 44919, South Korea*
[e] *School of Nanoscience and Technology, Indian Institute of Technology, Kharagpur, 721302, India*
[f] *Institute of Solid State Physics, University of Latvia, Riga, 1063, Latvia*
[g] *Department of Physics, Yangzhou University, Yangzhou, 225009, China*

ARTICLE INFO

Article history:
Received 14 May 2021
Received in revised form
21 June 2021
Accepted 22 June 2021
Available online 26 June 2021

Keywords:
Topological charge transport
Pressure-temperature phase-diagram
X-ray absorption
Charge-transfer complex

ABSTRACT

The hybrid inorganic/organic closed π-stacking and soft lattice of a copper anion radial (Copper-7,7,8,8-tetracyanoquinodimethane) renders its electrical conductivity and structural modifications, which are susceptible to temperature and pressure. The geometry of its metal-ligand construction contemplates the concept of topology with a charge-transfer instability. A pressure-induced ionic-neutral phase transition occurs and accompanies an anomalously large electrical conductivity, carries topological charges, and possesses a low energy gap smaller than the Coulomb gap. X-ray absorption spectroscopy of the metal establishes the high electrical conduction by the topological charges. X-ray diffraction and the first-principles calculations further suggest that the compression leads to an irreversible alteration in the metal coordination and rotation of the quinoid rings of the anion. The present observation demonstrates a close coupling of topological charges and lattice dynamics within a relatively low-pressure regime, which may expand a novel paradigm for the comprehensive topological charge transport phenomena including thermoelectric effects in future.

1. Introduction

In contrast to inorganic metals, the crystals of organic charge-transfer complexes with ordered stacked radicals present closed-shell structure with small transfer integral and large onsite Coulomb repulsion energy U coupled to their charge transport. Moreover, they have intermolecular orbital overlap resulting in an extremely narrow electronic bandwidth W. Thus, a large U/W ratio compels the radial based system to remain trapped in a Mott insulating state with unpaired isolated electrons [1–3]. Electronic criteria to advance the charge transport is conceptually simple, but practically challenging. Hubbard model predicts a metallic ground state based on a half-filled band ($s = 1/2$ system) must require $W > U$, as observed in few highly conductive frameworks [3]. An alternative approach is to include heavy heteroatom in radical-based materials that satisfies $W > U$. This inclusion inevitably increases the tendency of dimerization and leads to a subsequent quenching of spin and charge carriers which further results in a Peierls distorted insulating or weakly semiconducting ground state [4]. Hence, the challenge that persists for improvements in conductivity requires to reduce U, increase W, and prevent dimerization.

The charge transfer (CT) compounds are appealing because, under compression with gigapascal pressures, they exhibit dramatic modifications of electronic and structural states of matter [5–13]. Indeed, compression increases intermolecular interaction, contracts the lattice, and originates a local potential which intends to localize the electrons. Such a self-trapping phenomenon is enabling comprehensive views into the basic electron-phonon coupling (EPC) process where pressure probes EPC and its

---

* Corresponding author.
E-mail address: linwang@ysu.edu.cn (L. Wang).

https://doi.org/10.1016/j.mtphys.2021.100467
2542-5293/© 2021 Published by Elsevier Ltd.

localization mechanism. The electronic response of CT compounds ranges from strong EPC (insulating) to weak EPC (metallic) mechanisms. However, the intermediate coupling (IC) range remains highly intriguing and demonstrates insulator- or semiconductor-metal transition (IMT or SMT) where pressure modifies the transition temperature T_{IM} by forcing effective W ($W_{eff} \propto T_{IM}$) to change.

The quasi-one dimensional π-stack anion radical complex like Copper-7,7,8,8-tetracyanoquinodimethane (Cu-TCNQ) [14–16] is a prototype CT compound which exhibits semiconducting ground state along with a Peierls distortion [17,18] at low temperature. Apart from its advanced applications [19,20], we successfully reveal a pressure-driven metallization process by tuning the degree of band occupation (lower U and increase W) accompanying an ionic-neutral phase transition. In the ionic phase, cations possess a fully occupied electron shell without any spin state. Across the phase transition to the neutral state, the spin degrees of freedom could be activated under pressure by spin-singlet formation in absence of dimerization. Therefore, we argue that pressure subsequently triggers the emergence of current carrying topological excitons [21]. The presence of such excitons in form of neutral anions (A^0) was reported in tetrathiafulvalene-p-chloranil (TTF-CA) crystal [22] where photoexcitation created "excess charge" and delocalized. Therefore, the increase of conductivity with low temperature and pressure in Cu-TCNQ may involve the propagation of charge and spin solitons with a subtle balance of fluctuations between lattice and electronic energies. Considering its general softness (elasticity and high compressibility) and allowing the thermodynamic responses (phase stability and transition), the exotic electronic properties of this CT compound can organize an interesting platform to study its structural and physical properties under external hydrostatic pressure.

2. Results

2.1. Enhancement of electrical conductivity and semiconductor-to-metal transition

We sealed Cu-TCNQ nanowires along with the platinum (Pt) electrodes in a diamond-anvil-cell (DAC) to perform in-situ quasi-hydrostatic pressure dependent studies. They demonstrate a wide range of physical properties as a response to pressure, and electrical conductivity is one of them. First, we present a pressure-temperature ($P-T$) phase diagram in Fig. 1(a) up to 30 GPa constructed on the basis of resistivity ($R-T$) profiles in Fig. 1(b). These profiles are distinctly different below and above 0.7 GPa. Below 0.7 GPa, a strong insulating behavior is pronounced at low temperature indicating the presence of a large and robust charge gap against pressure. For pressures above 0.7 GPa, the ambient semiconducting state is gradually suppressed and SMT occurs at temperature T_{SE} defined by the kink in $R-T$ curve (Fig. 1(b): inset). A contour plot of the resistivity (Fig. 1(a)) illustrates an emergence of highly conducting state. The resistivity steeply rises for $T < T_{SE}$ where SMT only visible at high temperatures 240 K $< T <$ 300 K and survives up to 13 GPa. For this narrow temperature region, resistance follows power-law behavior $R(T) \propto T^{\varsigma}$ with $0 < \varsigma < 1$ and rules out the possibility of the Fermi liquid ($\varsigma = 2$) and Bloch-Grüneisen theory of electron-phonon scattering $\varsigma = 1$. The shifting of T_{SE} towards the low temperature with increasing pressure clearly infers about a significant contribution from the pressure-driven weakening of EPC, i.e., considerable broadening of W_{eff}. The conduction mechanism is further characterized by the Efros-Shklovskii variable range hopping (ESVRH) model (Fig. 1(c)) as $R = R_0 \exp\left[\left(\frac{T_0}{T}\right)^{1/2}\right]$ where $T_0 = 2.8e^2/(\varepsilon k_B \xi)$ is the ESVRH characteristic temperature as coupled to the localization length (ξ) and dielectric constant (ε) of the material [23]. In typical semiconductors, ξ grows (Fig. 1(d)) with the increasing electron concentration n and reduces T_0. Here, T_0 reaches to the minimum around 10 GPa (Fig. 1(c): inset). Fig. 2 shows the pressure dependence of resistivity expressed in terms of current-voltage ($I-V$) characteristics and illustrates that a highly conducting state is appearing around 10 GPa. The compression-induced non-linear conductivity demonstrates an ON-state with a strikingly high current ~10^2 mA for a low applied pressure ~1.0 GPa (Fig. 1(a)) (Supplementary Materials: Section S1 and Fig. S1(a)). For a critical pressure $P_c = 1.1$ GPa and positive (negative) bias sweep, current rapidly switches from an OFF-state (HRS: high resistive state) to an ON-state (LRS: low resistive state) at a threshold voltage V_{SET} (V_{RESET}). It is remarkable that the conductivity is enhanced by ~10^3 (10^2) times from its ambient value at 1.0 (0.5) GPa even with a low applied bias (Fig. 2(b)) for Cu-TCNQ phase-I (phase-II, Supplementary Materials: Fig. S1).

The conductivity rises steeply up to 8.0–9.0 GPa and a high-conducting state sustains without any distinct ON-OFF states (Fig. 2(b)). The pressure-driven SMT (conductivity maximum in Fig. 1(c)) indicates that donor to acceptor charge transfer is not only confined in the transition region, but also defined by the nature of the bonds. In comparison with other alkali-metal-TCNQ salts [24], Cu-TCNQ phase-I demonstrates the lowest transition pressure for SMT (Fig. 2(c): inset). Phase-II converts to phase-I via an unstable phase-III [25] at the expense of bond breakage, their rearrangements, and a formation of new Cu—N coordination bonds and therefore, delays the transition [16]. Due to organic-framework's soft nature, application of ultra-high pressure causes an irreversible change in it; thus fails to regain the original structure and conductivity starts to decrease significantly above 12 GPa (16 GPa, phase-II) (Fig. 2(c)). The recovery of conductivity after pressure release on Cu-TCNQ structures is only applicable below SMT.

2.2. Coulomb gap and charge localization

At ambient pressure and $T <$ 100 K, non-linear conductance and a CDW transport was manifested by Peierls transitions [17]. We observed that the exchange of energy between lattice and electrons promotes the delocalization of carriers and thus explains the high conducting states [26]. The improved nanoscopic intra- ($t_{||}$) and inter-molecular ($t_{\perp}$) transfer integrals between the donor and acceptor molecules clearly explain the weaker localization with reduction of T_0 which is further reduced to Coulomb gap $\Delta_{CG} = k_B\sqrt{T_0 T_{SE}}$ at Fermi level (Fig. 1(d)). We assume ESVRH conduction process emerges at the temperature T_{SE} when activation energy for nearest neighbor hoping becomes equal to Δ_{CG}. An exponential shrinkage of Δ_{CG}assures the highest conductivity around 10 GPa. There might exist different transfer integrals between the nearest neighbor chains (t_1 : Cu—4N$_1$ and t_2 : Cu—2N$_2$) and the system remains trapped to the insulating state for $t_1 = t_2 = 0$. For a large value of t_{12} (Cu—6N), charge gap collapses, and a metallic state emerges. A more rigorous calculation of ξ connects the hopping length as $l_h = (\xi/4)(T_0/T)^{1/2}$ yielding an estimated l_h(20 K, 10 GPa) ~ 12 nm. Taking carrier density $n_{CuTCNQ} = 2.34 \times 10^{24}/\mathrm{m}^3$, the mean distance between two hopping sites is $\frac{r}{2} = [3/(4\pi n_{CuTCNQ})]^{1/3}$ ~5 nm. At the lowest possible temperature, r is of the same order with l_h signifying the electron localizations below T_{SE}. The long-range Coulomb interactions of the localized electrons could only create a soft energy gap for low

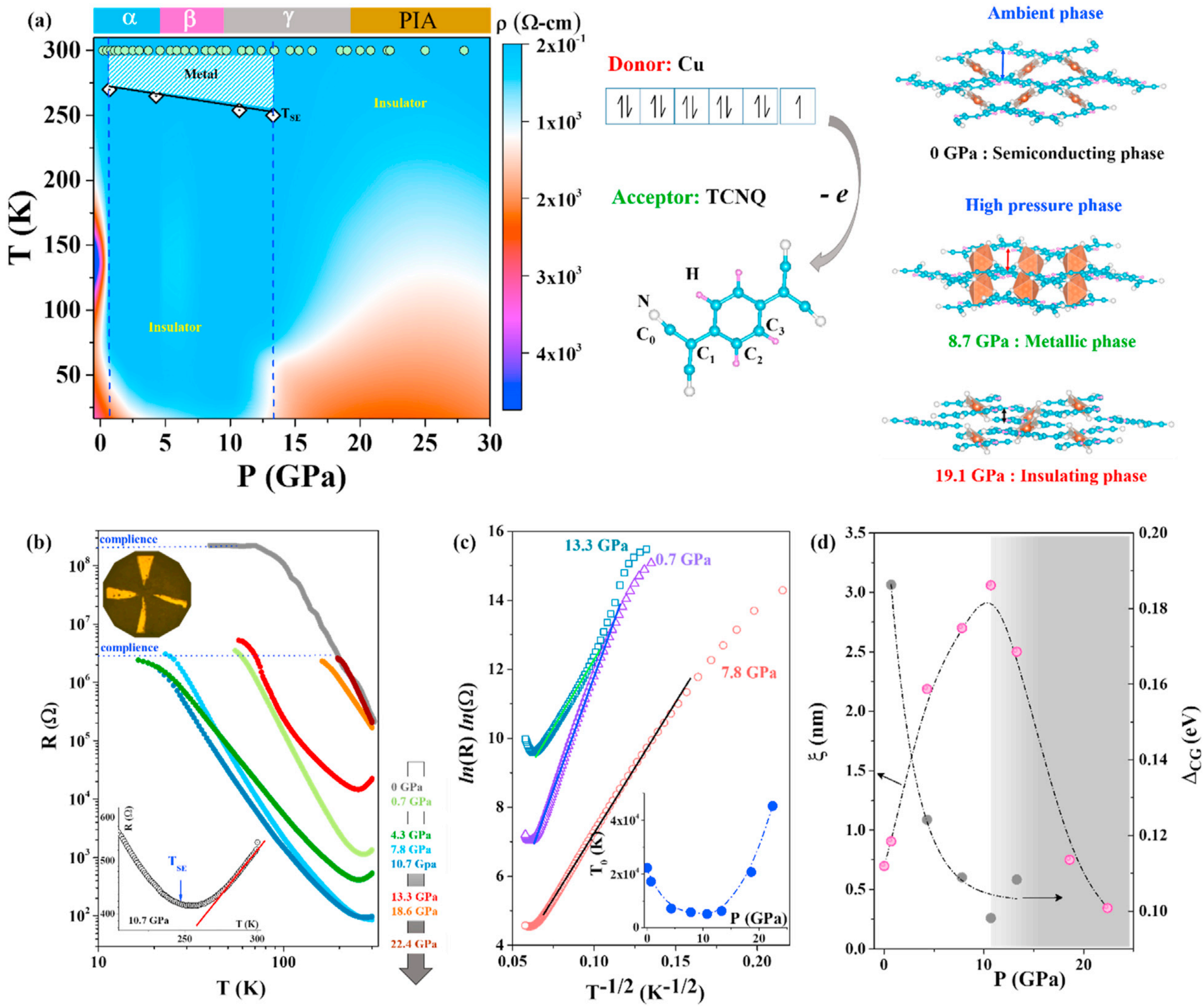

Fig. 1. (Color online) Phase-temperature phase diagram of Cu-TCNQ and resistivity profiles. (a) Pressure-temperature ($P-T$) phase diagram consisting of three different electronic phases in Cu-TCNQ, namely semiconducting (ambient) (left), metallic (8.7 GPa), and insulating (19.1 GPa) phases (top right). The metal donor atom Cu and acceptor TCNQ molecules form Cu-TCNQ stacks (top left). The white squares are the positions of the kinks (T_{SE}) in resistivity profiles shown in **(b)** which correspond to the semiconductor-metal transition temperatures. The green solid circles indicate the pressure-dependent resistivity data at ambient temperature. α, β, γ, and pressure-induced amorphization (PIA) correspond to four crystallographic phases at ambient temperature. **(c)** The ESVRH model fitting for $R-T$ curves for few pressure points along with the pressure evolution of **(d)** ξ and Δ_{CG} (see text).

pressure and temperature $T < T_{SE}$. For $P >$ 14 GPa, the structural disorders and later pressure-induced amorphization (PIA) strengthen the localization effects, make the EPC stronger, and revive an insulating state. However, it might be hard to achieve a metallic ground state (0 K) without destroying the molecular structure.

2.3. Pressure effect on the local atomic and electronic structure

Synchrotron X-ray absorption spectroscopy (XAS) in Fig. 3 reveals the chemical state and coordination geometry in Cu-TCNQ at room temperature. The Cu K-edge of X-ray absorption near-edge structures (XANES) in Cu-TCNQ at low pressures (5 and 9 GPa) exhibit a distinct peak at about 8981.5 eV attributed to the dipole-allowed Cu 1s → 4p transition [27]. At larger pressures, the peak is masked by the overlapping EXAFS oscillations due to the pressure-induced changes in the atomic structure upon amorphization (Fig. 3(a)). The position of the copper absorption edge determined as a first derivative of the absorption coefficient shifts by about 0.5 eV to lower binding energies upon compression (Fig. 3(a): inset). Therefore, it suggests a slight decrease in the copper oxidation state from Cu^{+} towards Cu^{0} due to the changes in the overall charge density under compression [28]. Note that even at the highest pressure of 27.8 GPa, the position of the copper edge for Cu-TCNQ is located about 1 eV above the edge for the reference copper foil.

The pressure-dependence of the EXAFS oscillations (Fig. 3(b)) indicate that the main EXAFS frequency, determined by the nearest atoms, remains nearly unchanged. The high-frequency contributions due to the next groups of atoms vary significantly, especially at the highest pressure of 27.8 GPa. These effects can be better evidenced in the *R*-space (Fig. 3(c)), where pressure-induced changes of interatomic distances are clearly visible. While the first peak position remains unchanged at all pressures, the second one shifts from about 2.6 Å to 2.3 Å upon increasing pressure to 27.8 GPa. In a highly distorted tetrahedral environment [14], the nitrogen atoms (N_1) are the main responsible for the first peak in FTs. Other two nitrogen atoms (N_2) and four carbons (C_3) located at longer distances contribute to the first and second peaks in FTs, respectively. The pressure dependence of the average interatomic

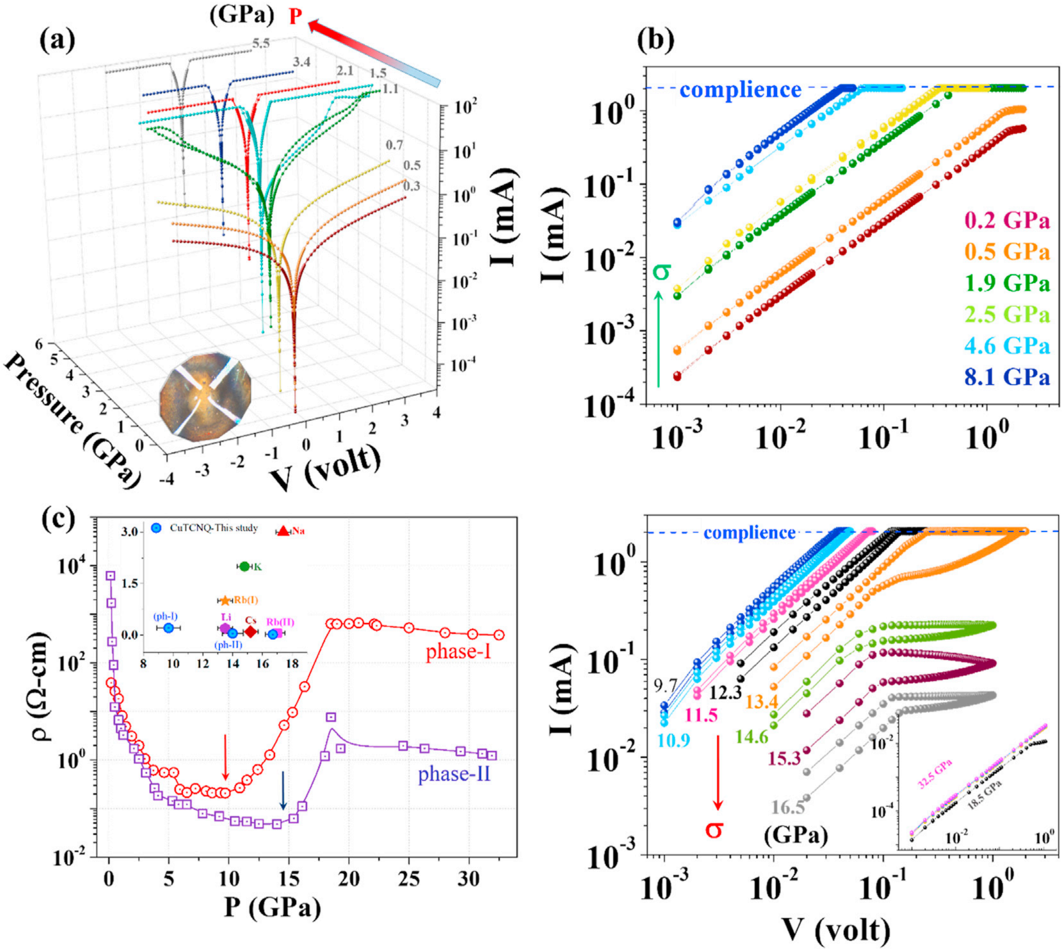

Fig. 2. (Color online) Pressure-dependent non-linear conductivity of Cu-TCNQ at room temperature. (a) $I-V$ characteristics show non-linear conductivity including HRS-LRS switching of under compression. The conductivity (σ) first **(b)** increase (top panel) and then decrease (bottom panel) with pressure. **(c)** Pressure dependencies of resistivity for phase-I and phase-II. Inset shows the observed lowest transition pressures for Cu-TCNQ in comparison with other alkali metal-TCNQ crystals. The molecular arrangement of Cu-TCNQ in the *ab*-plane is shown.

distances R (Cu—N$_1$), R (Cu—N$_2$), and R (Cu—C$_3$) obtained from the best-fit analysis is reported in Fig. 3(d). Both groups of the Cu—N bonds demonstrate weak dependence on pressure; however, the Cu—C bonds become compressed at $P > 10$ GPa. Such behavior of interatomic distances suggests that nitrogen atoms play the role of joints allowing TCNQ ligands to rotate under compression. It may also allow distortion of the framework or modification in metal center coordination accompanying successive phase transitions to lower symmetric phases from its ambient monoclinic *Pn* phase (Supplementary Materials: Fig. S2, Fig. S3, and Fig. S4). Pressure-induced volume reduction in Fig. 4 (a) occurs due to a steep reduction of *c*-axis (ease of compression of π-stacks) compared to a monotonic decrease of *a* and *b* axes (Fig. 4(b)). The in-plane closely packed C≡N bonds along $a-b$ planes may accommodate a greater compression resulting in an anisotropic compression in the lattice.

2.4. Coordination of donor atoms, change in bond order, and charge transfer

By comparing the three molecular structures (Fig. 1(a)), the drastic pore volume reduction necessitates the accommodation of tilting/distortion of the metal coordination polyhedral confirmed by the cation coordination changes from tetrahedral to octahedral (Fig. 1(a)) around 8.7 GPa. In this denser phase, the average Cu—N$_1$ distance is 2.09 Å consistent with previous reports [16]. The two nearest N-atoms coordinated to the Cu-site are at the shortest distance of 1.91 Å, while the C—C bonds are strongly bent, but the C-rings remain parallel at 3.47 Å apart. The vibrational modes corresponding C=C—H bending and C—C≡N stretching frequencies (Supplementary Materials: Fig. S5) demonstrate distinct changes with pressure and the population of electrons in TCNQ increases with decreasing lengths of these bonds [29,30]. Their dominant role in electrical conductivity is estimated by the degree of charge transfer (DCT) from donors to acceptors and is a linear correlation with cyano-vibrational mode as $DCT = 2(\delta\nu/\nu_0)(1-\nu_1^2/\nu_0^2)$ where $\delta\nu = \nu_0 - \nu_{CT}$, and ν_0, ν_{CT}, ν_1 represent selective stretching modes of a pure acceptor, charge transfer compound, and acceptor anion respectively. The fractional $DCT = 0.5$ at ambient condition with localized electrons within frameworks decreases with pressure (Supplementary Materials: Fig. S6). The exocyclic double bonds become short and reduce their bond order due to the loss of certain degrees of rotational freedom under compression [16]. The anisotropic repercussions of unit cell contraction are likely to encompass a disruption of the CT mechanism in the approach of orbital overlap and preference of the neutral states of Cu^0 and TCNQ^0 (Fig. 4(a)).

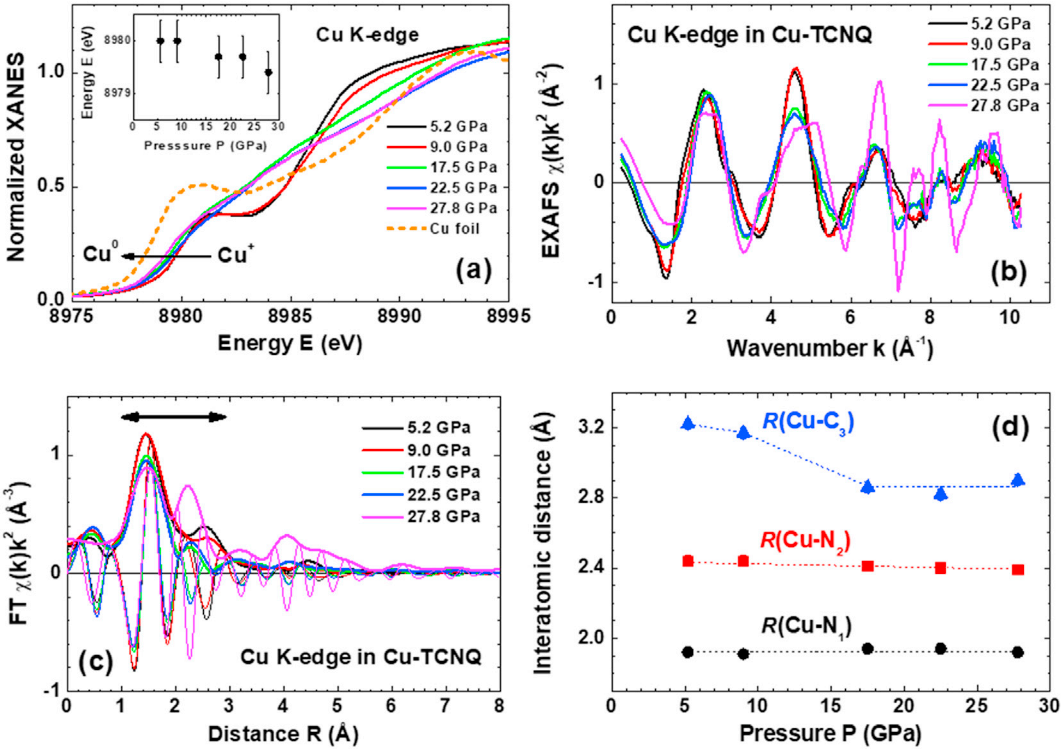

Fig. 3. (Color online) X-ray absorption spectroscopy under pressure. **(a)** Normalized Cu K-edge X-ray absorption near-edge structures (XANES) for Cu-TCNQ and Cu foil. Inset shows the pressure dependence of the absorption edge position determined as a first derivative of the absorption coefficient. The Cu K-edge EXAFS spectra $k^2\chi(k)$ **(b)** and their Fourier transforms (moduli and imaginary parts) **(c)** for Cu-TCNQ at different pressures. Note that the position of peaks in FTs differs from the true crystallographic values due to the presence of the scattering amplitude and phase shift contributions in the EXAFS spectra. The range of data analysis is indicated in (c) by the arrow. **(d)** Pressure dependence of the average interatomic distances R (Cu—N$_1$), R (Cu—N$_2$) and R (Cu—C$_3$). Dotted lines are guides for the eye.

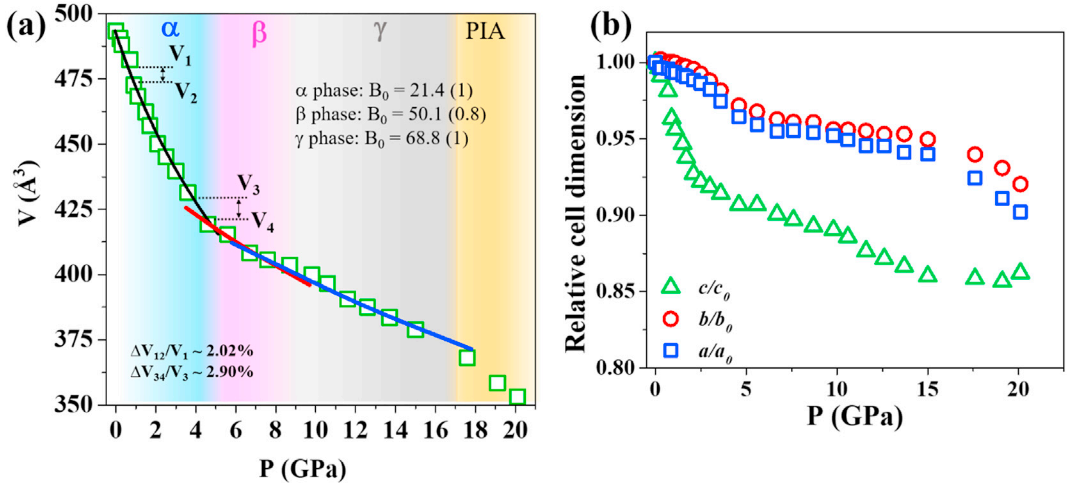

Fig. 4. (Color online) Structural transition under pressure. (a) Unit cell volume vs. pressure plot for α-, β-, and γ-phases fitted with second-order Birch-Murnaghan equation of state (solid lines). The low elastic modulus and their pressure-induced softening establish a direct correlation between instability and PIA [44]. **(b)** Evolution of the normalized lattice parameters show anisotropic compression of unit cells.

2.5. Electronic band structure and collapse of band gap

The projected density of states (PDOS) and the electronic band structure are displayed in Fig. 5 shows the valence band maxima (VBM) crosses the Fermi level for all pressures considered. The result is highly consistent with earlier theoretical investigation [15] at ambient condition. In PDOS, Cu-3d, C-2p and N-2p orbitals form VBM, whereas contribution to CBM comes from C-2p and N-2p orbitals (Fig. 5(a) and Fig. S7). Demonstrating an indirect to direct band gap transition, the experimental (theoretical) band gap shows a red shift up to cross over region around 11.7 GPa and reaches to its minimum value ~ 1.3 (0.8) eV (Fig. 5(b)). It also confirms the emergence of a metallic state under pressure. A strong compression leads to highly distorted structure, bending of chemical bonds, fragmentation of organic layers, and successive lower symmetric structural transitions. Therefore, few available energy states are

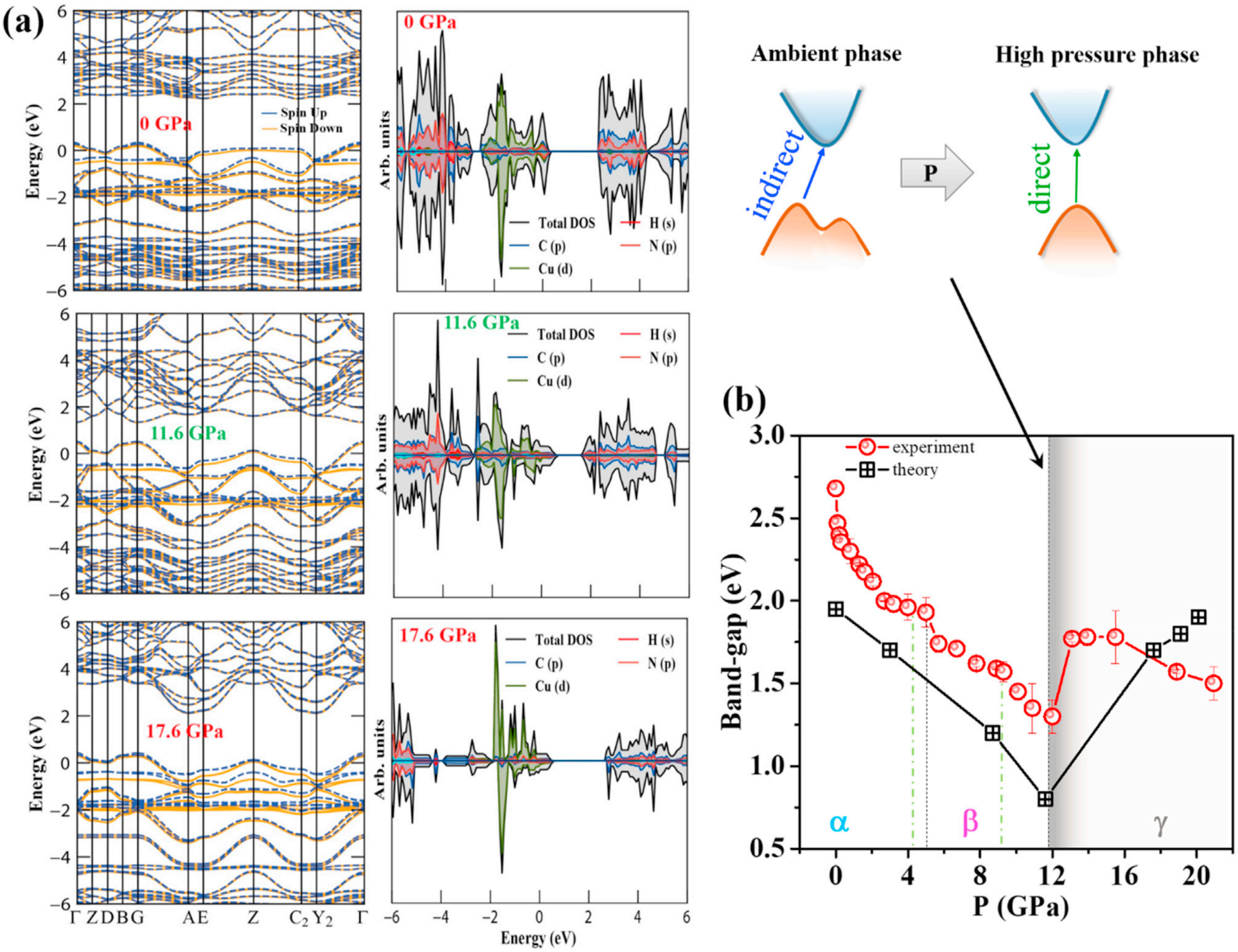

Fig. 5. (Color online) Evolution of band structure with pressure. (a) Calculated PDOS on each atom in Cu-TCNQ and the corresponding band structures at few representative pressure values. At ambient pressure, the calculated energy gap between VBM and CBM is 1.95 eV, which is slightly less than experimental value (2.6 eV) due to the unavoidable underestimations of the band gap by GGA (DFT-PBE) exchange-correlation functionals. **(b)** The optical band gap derived from the experimental absorption data is compared with the theoretical indirect/direct band gap as a function of pressure. Green dashed lines show the structural phase transitions as derived from XRD data and lower than the values obtained from band gap calculations (black dotted lines).

available to support an indirect band gap at high pressure.

3. Discussion

3.1. Our results provide insights into topological charge transport

Cu-TCNQ is a radical anion salt and displays a strong ionic character at ambient condition [14,15] and the cation has fully occupied electron shell (no spin), whereas the lowest unoccupied molecular orbital (LUMO) of TCNQ molecule is empty. They possess segregated donor (D) and acceptor (A) stacks with partial charge transfer δ from donor Cu to acceptor TCNQ schematically depicted in Fig. 6(a). The partial charge transfer from Cu to TCNQ occurs due to strong hybridization of the orbitals and a semiconducting state with low-bandwidth prevails. However, upon compression, shrinkage of lattice and bond lengths corroborate significant broadening of the bandwidth and consequent redshift of the band gap (Fig. 5) at ambient temperature. However, to explain the emergence of metallic states at low pressure and relatively high temperature ($T > T_{SE}$), we propose the generation of topological excitations. They are solitons; they become active and competes with structural fluctuations resulting a decrease (increase) of resistance (conductivity) (Fig. 2(b)). These current-carrying topological charges are originating from a charge inhomogeneity at the critical pressure $P_C \sim 1$ GPa (Fig. 3(a)) and can be excited with relatively lower excitation energies than Δ_{CG}. Therefore, few TCNQ$^-$ anions may convert to neutral TCNQ^0 and start to propagate along TCNQ$^-$ columns as solitons and carry charge as shown in Fig. 6(b). The growing overlap among the wave functions of organic chains leads to the enhancement of the diffusive motion of the solitons and exhibits an increase of conductivity. The charge delocalization stabilizes with further compression [16] and ambient semiconducting phase is gradually suppressed.

As it was experimentally demonstrated, Cu$^+$ converts to the neutral Cu^0 around 10 GPa (Fig. 4(a)), the spin solitons develop in the high pressure phase. In the adjacent chains, a charge (spin) soliton can hop into a spin (charge) soliton site by donating electrons with a high d. c current (Fig. 2(a)). Recently, ^{13}C NMR (nuclear magnetic resonance) shift and relaxation rate (T_1^{-1}) analyses in TTF-CA also verified pressure-evolution of topological excitations like kinks at the paraelectric-ferroelectric (neutral-ionic (NI)) mobile domain walls (DWs) and charge-/spin-carrying solitons [31]. The authors proposed that sparsely excited spin solitons act like free spins in presence of negligible exchange interaction. A schematic in

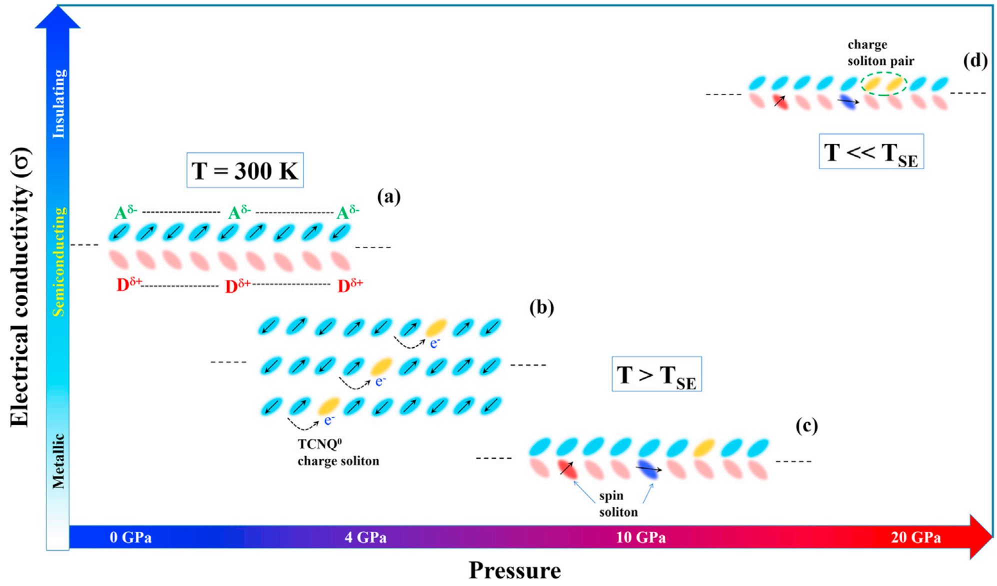

Fig. 6. (Color online) Topological excitations (solitons) and electrical conductivity evolution under compression. (a) D-A segregated stacking with partial charge transfer support semiconducting nature of Cu-TCNQ at ambient conditions. **(b)** For $T > T_{SE}$, at low pressure, few charge solitons propagate in organic stacks. **(c)** Around 10 GPa, charge and spin solitons become highly active and a metallic state emerges. **(d)** The soliton pairs are restricted to hop in the adjacent stacks and compels the system to return in an insulating state at very low temperatures and at high pressure.

Fig. 6(c) demonstrates the spin soliton excitation in D-A pairs in the SMT region for Cu-TCNQ. Thus, at low pressure, the conductivity is ruled by charge solitons and is handed over to conductivity by spin solitons (below 12 GPa). In TTF-CA [31], spin-solitons (polarons) sandwiched by NIDWs propagate in low-pressure neutral phase, while more densely charge solitons excited in high-pressure ionic phase. However, for both cases, the charge fluctuations are sensitive to thermal environment, and the occurrence of charge solitons decreases with decrease of temperature. Additionally, compression-induced lattice shrinkage couple the (±) soliton pairs (Fig. 6(d)) which do not find suitable way to hop in the adjacent stacks; and conductivity starts to decrease again.

3.2. *The principles described here possible to apply more broadly*

We unveiled a metallization process at low temperature and high pressure across an ionic-neutral phase transition in Cu-TCNQ. Pressure effectively tunes the EPC and reduces the U/W ratio significantly. Simple modeling and multimodal experiments conclude that the high conducting state via mobile topological excitons is enhanced under compression, in contrary to previous conventional electrical transport studies in metal-organic frameworks. Therefore, the interplay of lattice dynamics and pressure tuning of such transport paves way to a wide range of remarkable charge transport mechanisms. For example, it may be applicable to the recent development of the topological spin-dependent high performance new thermoelectric materials with interconnected nanowire networks [32].

4. Materials and methods

4.1. *Sample preparation*

The single crystalline Cu-TCNQ nanowires were synthesized by physical vapor deposition technique (Fig. S8). It can be derived into two stable structures (Fig. S9) as phase-I (monoclinic-*Pn*) and phase-II (monoclinic-*P2/n*) with high (0.25 S-cm^{-1}) and low (1.3 × 10^{-5} S-cm^{-1}) conductivities.

4.2. *In-situ high pressure experiments*

Electrical transport: In-situ high-pressure electrical conductivity was measured with a four-probe direct-current (d.c) method at ambient temperature in a symmetric DAC. The low-temperature electrical transport measurements were carried out in Physical Property Measurement System (PPMS) using Be—Cu screw drive DAC. The insulation between conducting leads and gaskets for both types were secured by compressing cubic boron nitride in the sample chamber. Thin platinum foils were used as conducting electrodes. No pressure transmitting medium (PTM) was used.

Structural characterizations: *In-situ* high-pressure synchrotron XRD experiments were conducted at ambient temperature at Shanghai Synchrotron Radiation Facilities (15U beamline with wavelength 0.6199 Å). A steel gasket (thickness ~ 40 μm, hole diameter 100 μm) and silicone oil was used as a PTM for the sample chamber. The 2-dimensional XRD data were integrated into one-dimensional profiles using the Dioptas program [33]. Le Bail fittings were carried out using the Jana2006 program [34] (Supplementary Materials: Section S2). The scanning electron microscopy image (Fig. S10) of recovered sample shows the change in packing density and increased dimensionality [35].

The high-pressure synchrotron x-ray absorption spectroscopy (XAS) experiments were performed at SPring-8 (BL05XU beamline). The synchrotron radiation from the in-vacuum undulator was monochromatized by a Si(111) monochromator, and higher harmonic X-rays were removed using Rh-coated mirrors. The energy scale was calibrated using copper foil. The sample was loaded without PTM in the DAC and was located between two ionization chambers. The Cu K-edge absorption spectra were collected in the transmission mode. The XAS data were analyzed by ATHENA [36] and XAESA [37] programs. The EXAFS spectra (Fig. 3(b)) were defined as $\chi(k) = (\mu(k) - \mu_0(k))/\Delta\mu_0$ after background removal where k is the photoelectron wavenumber, $\mu_0(k)$ is a smoothly varying absorption background, and $\Delta\mu_0$ is the absorption edge-jump. Their Fourier transforms (FTs) were calculated using the 10% Gaussian window-function (Fig. 3(c)). The contribution from the nearest atoms (6 N and 4C) around the absorbing copper was isolated by back-FT in the range of $R = 0.8–3.0$ Å and analyzed within the single-scattering harmonic approximation using the conventional EXAFS equation [38] (Support information: Section S3 Fig. S11).

4.3. Raman and UV–vis spectroscopy

Raman spectra were recorded with a Raman spectrometer (Ranishaw, model: inVia micro-Raman) equipped with a 633 nm HeNe laser (17 mW) and 1800 l/cm grating.

The high-resolution pressure-induced UV–vis spectroscopy measurements were carried out using a micro UV–vis spectroscopy system (DH-2000-BAL, Ocean Optics) using a symmetric DAC with type-II diamonds.

The pressure was calibrated by the regular ruby fluorescence method for all pressure-dependent studies.

4.4. Theoretical electronic band structure calculations

Spin-polarized density functional theory (DFT) calculations were performed using the plane-wave formalism as implemented in the Quantum-Espresso package [39] with the norm-conserving pseudopotentials [40,41]. We use generalized gradient approximation (GGA) with Perdew–Burke-Ernzerhof (PBE) [42] exchange and correlation functional. The core–valence interaction was described by the projector-augmented wave method and the Van der Waals dispersion correction of Grimme [43] was considered. Plane wave functions were expanded with an energy cutoff of 100 Ry and Brillouin zone sampled using $15 \times 15 \times 15$ gamma centered k-mesh. Structural relaxation was performed by fixing the lattice parameters to the experimental results and all atoms were fully relaxed (Supplementary Materials: Fig. S8 (c)).

Author contributions

S.S. and L.W. conceived the project. S.S. and L.W. designed and performed the electrical transport, XRD, and Raman experiments and analyzed the data. A.S.N. performed theoretical band-structure calculations. R.B. prepared nanowire samples for the experiments and performed TEM data analysis. M.T.L. collected XAS data at beamline. A.K. and S.S. conducted XAS data analysis. S.S., A.S·N., A.K., L.W., Y.J.T. and H–K.M. wrote the manuscript with inputs of all the authors.

Funding

This work was supported by Natural Science Foundation of China (Grant Nos. 52090020, 11874076). A.K. thanks the Institute of Solid State Physics, University of Latvia as the Center of Excellence has received funding from the European Union's Horizon 2020 Framework Programme H2020- WIDESPREAD-01-2016-2017-Teaming Phase2 under grant agreement No. 739508, project CAMART2. M.T.L. thanks the financial support from the Natural Science Foundation of China (Grant No. 11804011).

Declaration of competing interest

The authors declare that there is no conflict of interests.

Acknowledgments

We thank Kiyofumi Nitta and Oki Sekizawa for providing assistance on the setup for XAFS measurements under proposal No. 2018A1760 at BL05XU, Spring-8, Japan.

Appendix A. Supplementary data

Supplementary data to this article can be found online at https://doi.org/10.1016/j.mtphys.2021.100467.

References

[1] H. Kojima, Z. Zhang, K.R. Dunbar, T. Mori, Energy band structure and metal-organic interactions in tetracyanoquinodimethane (TCNQ) and N,N'-dicyanoquinonediimine (DCNQI) materials, J. Mater. Chem. C 1 (2013) 1781–1790.

[2] M. Mitrano, G. Cotugno, S.R. Clark, R. Singla, S. Kaiser, J. Stahler, R. Beyer, M. Dressel, L. Baldassarre, D. Nicoletti, A. Perucchi, T. Hasegawa, H. Okamoto, D. Jaksch, A. Cavalleri, Pressure-dependent relaxation in the photoexcited mott insulator ET-F2TCNQ: influence of hopping and correlations on quasi-particle recombination rates, Phys. Rev. Lett. 112 (2014), 117801.

[3] Y. Yoshida, H. Kitagawa, One-dimensional electronic systems: metal-chain complexes and organic conductors, Chem. Commun. 56 (2020) 10100–10112.

[4] R.E. Peierls, Quantum Theory of Solids, Oxford University Press, London, 2001.

[5] H. Cui, T. Tsumuraya, T. Miyazaki, Y. Okano, R. Kato, Pressure-induced metallic conductivity in the single-component molecular crystal [Ni(dmit)2], Eur. J. Inorg. Chem. (2014) 3837–3840 (2014).

[6] D.S. Chow, P. Wzietek, D. Fogliatti, B. Alavi, D.J. Tantillo, C.A. Merlic, S.E. Brown, Singular behavior in the pressure-tuned competition between spin-peierls and antiferromagnetic ground states of (TMTTF)2PF6, Phys. Rev. Lett. 81 (1998) 3984–3987.

[7] J.W.L. Wong, A. Mailman, K. Lekin, S.M. Winter, W. Yong, J. Zhao, S.V. Garimella, J.S. Tse, R.A. Secco, S. Desgreniers, Y. Ohishi, F. Borondics, R.T. Oakley, Pressure induced phase transitions and metallization of a neutral radical conductor, J. Am. Chem. Soc. 136 (2014) 1070–1081.

[8] A. Andrieux, H.J. Schulz, D. Jerome, K. Bechgaard, Conductivity of the one-dimensional conductor tetrathiafulvalene-tetracyanoquinodimethane (TTF-TCNQ) near commensurability, Phys. Rev. Lett. 43 (1979) 227–230.

[9] A. Jaffe, Y. Lin, W.L. Mao, H.I. Karunadasa, Pressure-induced conductivity and yellow-to-black piezochromism in a layered Cu-Cl hybrid perovskite, J. Am. Chem. Soc. 137 (2015) 1673–1678.

[10] Q. Sui, X.T. Ren, Y.X. Dai, K. Wang, W.T. Li, T. Gong, J.J. Fang, B. Zou, E.Q. Gao, L. Wang, Piezochromism and hydrochromism through electron transfer: new stories for viologen materials, Chem. Sci. 8 (2017) 2758–2768.

[11] K.W. Chapman, G.J. Halder, P.J. Chupas, Pressure-induced amorphization and porosity modification in a Metal–Organic framework, J. Am. Chem. Soc. 131 (2009) 17546–17547.

[12] F.-X. Coudert, Responsive metal–organic frameworks and framework materials: under pressure, taking the heat, in the spotlight, with friends, Chem. Mater. 27 (2015) 1905–1916.

[13] S. Wang, Q. Wang, X. Feng, B. Wang, L. Yang, Explosives in the cage: metal-organic frameworks for high-energy materials sensing and desensitization, Adv. Mater. 29 (2017).

[14] R.A. Heintz, H. Zhao, X. Ouyang, G. Grandinetti, J. Cowen, K.R. Dunbar, New insight into the nature of Cu(TCNQ): solution routes to two distinct polymorphs and their relationship to crystalline films that display bistable switching behavior, Inorg. Chem. 38 (1999) 144–156.

[15] M.J. Capitan, J. Alvarez, F. Yndurain, Organometallic MTCNQ films: a comparative study of CuTCNQ versus AgTCNQ, Phys. Chem. Chem. Phys. 20 (2018) 21705–21715.

[16] R. Caputo, S. Demir, A. Tekin, First-principles crystal structure prediction of Cu(I)-TCNQ polymorphs, J. Phys. Chem. C 124 (2019) 70–82.

[17] R. Basori, A.K. Raychaudhuri, Low temperature transport of a charge transfer complex nanowire grown with an electric field from the vapour phase, RSC Adv. 5 (2015) 86497–86504.

[18] M. Kumar, B.J. Topham, R. Yu, Q.B.D. Ha, Z.G. Soos, Magnetic susceptibility of alkali-tetracyanoquinodimethane salts and extended Hubbard models with bond order and charge density wave phases, J. Chem. Phys. 134 (2011), 234304.

[19] R.S. Potember, T.O. Poehler, R.C. Benson, Optical switching in semiconductor organic thin films, Appl. Phys. Lett. 41 (1982) 548–550.

[20] R. Basori, K. Das, P. Kumar, K.S. Narayan, A.K. Raychaudhuri, Large photo-response of Cu:7,7,8,8-tetracyanoquinodimethane nanowire arrays formed as aligned nanobridges, Appl. Phys. Lett. 102 (2013): 061111.

[21] J.L. Bredas, B. Themans, J.M. Andre, R.R. Chance, R. Silbey, The role of mobile organic radicals and ions (solitons, polarons and bipolarons) in the transport properties of doped conjugated polymers, Synth. Met. 9 (1984) 265–274.

[22] T. Suzuki, T. Sakamaki, K. Tanimura, S. Koshihara, Y. Tokura, Ionic-to-neutral phase transformation induced by photoexcitation of the charge-transfer band in tetrathiafulvalene-p-chloranil crystals, Phys. Rev. B 60 (1999) 6191–6193.

[23] S. Samanta, A.K. Raychaudhuri, Y.M. Mukhovskii, Non-Gaussian resistance noise in the ferromagnetic insulating state of a hole-doped manganite, Phys. Rev. B 85 (2012): 045127.

[24] I. Shirotani, A. Onodera, N. Sakai, Electrical behavior of alkali metal cation–TCNQ anion radical simple salts under very high pressures, Bull. Chem. Soc. Jpn. 48 (1975) 167–170.

[25] C.A. Fernandez, P.C. Martin, T. Schaef, M.E. Bowden, P.K. Thallapally, L. Dang, W. Xu, X. Chen, B.P. McGrail, An electrically switchable metal-organic framework, Sci. Rep. 4 (2014), 6114.

[26] S. Yasuzuka, K. Murata, T. Arimoto, R. Kato, Temperature-pressure phase diagram in TTF-TCNQ: strong suppression of charge-density-wave state under extremely high pressure, J. Phys. Soc. Jpn. 76 (2007), 033701-033701.

[27] B. You, X. Liu, G. Hu, S. Gul, J. Yano, D.-e. Jiang, Y. Sun, Universal surface engineering of transition metals for superior electrocatalytic hydrogen evolution in neutral water, J. Am. Chem. Soc. 139 (2017) 12283−12290.

[28] A.I. Frenkel, Q. Wang, N. Marinkovic, J.G. Chen, L. Barrio, R. Si, A.L. Cámara, A.M. Estrella, J.A. Rodriguez, J.C. Hanson, Combining X-ray absorption and X-ray diffraction techniques for in situ studies of chemical transformations in heterogeneous catalysis: advantages and limitations, J. Phys. Chem. C 115 (2011) 17884−17890.

[29] H. Jiang, P. Hu, J. Ye, K.K. Zhang, Y. Long, W. Hu, C. Kloc, Tuning of the degree of charge transfer and the electronic properties in organic binary compounds by crystal engineering: a perspective, J. Mater. Chem. C 6 (2018) 1884−1902.

[30] C. Sun, H. Zhao, C. Liu, M. Zhou, Pressure-induced Fermi resonance between fundamental modes in 7,7,8,8-tetracyanoquinodimethane, J. Raman Spectrosc. 48 (2017) 1127−1131.

[31] R. Takehara, K. Sunami, K. Miyagawa, T. Miyamoto, H. Okamoto, S. Horiuchi, R. Kato, K. Kanoda, Topological charge transport by mobile dielectric-ferroelectric domain walls, Sci. Adv. 5 (2019) eaax8720.

[32] N. Marchal, T. da Camara Santa Clara Gomes, F. Abreu Araujo, L. Piraux, Large spin-dependent thermoelectric effects in NiFe-based interconnected nanowire networks, Nanoscale research letters 15 (2020), 137.

[33] C. Prescher, V.B. Prakapenka, DIOPTAS: a program for reduction of two-dimensional X-ray diffraction data and data exploration, High Pres. Res. 35 (2015) 223−230.

[34] P. Václav, D. Michal, P. Lukáš, Crystallographic computing system JANA2006: general features, Z. für Kristallogr. - Cryst. Mater. 229 (2014) 345−352.

[35] S. Samanta, Q. Li, B. Cheng, Y. Huang, C. Pei, Q. Wang, Y. Ma, L. Wang, Phase coexistence and pressure-temperature phase evolution of VO_2(A) nanorods near the semiconductor-semiconductor transition, Phys. Rev. B 95 (2017), 045135.

[36] B. Ravel, M. Newville, ATHENA, ARTEMIS, HEPHAESTUS: data analysis for X-ray absorption spectroscopy using IFEFFIT, J. Synchrotron Radiat. 12 (2005) 537−541.

[37] A. Kalinko, XAESA v0.03. https://github.com/aklnk/xaesa, 2020.

[38] A. Kuzmin, J. Chaboy, EXAFS and XANES analysis of oxides at the nanoscale, IUCrJ 1 (2014) 571−589.

[39] P. Giannozzi, S. Baroni, N. Bonini, M. Calandra, R. Car, C. Cavazzoni, D. Ceresoli, G.L. Chiarotti, M. Cococcioni, I. Dabo, A. Dal Corso, S. de Gironcoli, S. Fabris, G. Fratesi, R. Gebauer, U. Gerstmann, C. Gougoussis, A. Kokalj, M. Lazzeri, L. Martin-Samos, N. Marzari, F. Mauri, R. Mazzarello, S. Paolini, A. Pasquarello, L. Paulatto, C. Sbraccia, S. Scandolo, G. Sclauzero, A.P. Seitsonen, A. Smogunov, P. Umari, R.M. Wentzcovitch, QUANTUM ESPRESSO: a modular and open-source software project for quantum simulations of materials, J. Phys. Condens. Matter 21 (2009), 395502.

[40] D.R. Hamann, Optimized norm-conserving Vanderbilt pseudopotentials, Phys. Rev. B 88 (2013), 085117.

[41] P. Scherpelz, M. Govoni, I. Hamada, G. Galli, Implementation and validation of fully relativistic GW calculations: spin−orbit coupling in molecules, nanocrystals, and solids, J. Chem. Theor. Comput. 12 (2016) 3523−3544.

[42] J.P. Perdew, K. Burke, M. Ernzerhof, Generalized gradient approximation made simple, Phys. Rev. Lett. 77 (1996) 3865−3868.

[43] S. Grimme, Semiempirical GGA-type density functional constructed with a long-range dispersion correction, J. Comput. Chem. 27 (2006) 1787−1799.

[44] L. Bouëssel du Bourg, A.U. Ortiz, A. Boutin, F.-X. Coudert, Thermal and mechanical stability of zeolitic imidazolate frameworks polymorphs, Apl. Mater. 2 (2014), 124110.